Supporting Information

**Hetero-nanojunction armored with carbon layer for boosting water oxidation over RuO$_2$ in acid**

Fanfan Shang [a], Huijie He [a], Yuan Lin [a], Bei An [a], Hairui Cai [a, b, c], Xiaoqian Li [a], Weitong Wang [a], Chao Liang [a, b, c, *], Shengchun Yang [a, b, c, *], Bin Wang [a, b, c, *]

[a] MOE Key Laboratory for Non-equilibrium Synthesis and Modulation of Condensed Matter, Key Laboratory of Shaanxi for Advanced Materials and Mesoscopic Physics, State Key Laboratory for Mechanical Behavior of Materials, School of Physics, Xi'an Jiaotong University, No. 28 West Xianning Road, Xi'an 710049, China

[b] National Innovation Platform (Center) for Industry-Education Integration of Energy Storage Technology, Xi'an Jiaotong University, No. 28 West Xianning Road, Xi'an 710049, China

[c] Shaanxi Collaborative Innovation Center for Hydrogen Fuel Cell Performance Improvement, Xi'an Jiaotong University, No. 28 West Xianning Road, Xi'an 710049, China

E-mail: chaoliang@xjtu.edu.cn; ysch1209@mail.xjtu.edu.cn; bin_wang@xjtu.edu.cn

## Chemicals

Ruthenium acetylacetonate (Sinopharm Chemicals), Cobalt acetylacetonate (Sinopharm Chemicals), DMF (Aladdin Reagent), Oleylamine (Aladdin Reagent), and oxalic acid (Aladdin Reagent) were all purchased. All chemicals were utilized without further purification. Milli-Q water of 18.2 MΩ·cm was used in all experiments.

## Experimental Section

**The synthesis of electrodes:** Firstly, the Ti felt with a size of $1 \times 0.5$ cm$^2$ was pre-treated in 10 wt% $H_2C_2O_4$ solution at 75 $^oC$ for 1 h. The obtained acid-treated Ti felt was washed with water under ultrasonication several times and dried in an oven at 60 °C. Secondly, 1.78 mg cobalt acetylacetonate and 2.5 mg ruthenium acetylacetonate were dissolved in a 0.1 mL DMF. Then, 0.4 mL oleylamine was added to a 0.1 mL DMF solution that contained 1.78 mg cobalt acetylacetonate and 2.5 mg ruthenium acetylacetonate, and sonicated for 10 min. Thirdly, 25 μL and 50 μL of the prepared precursor solution were dropped on the acid-treated Ti felt in two separate steps, each of which was calcinated at 400 $^oC$ for 2 h in a muffle furnace. After calcination, the obtained samples were rinsed with deionized water several times, dried in an oven at 60 °C, and assigned as $(Co_3O_4|RuO_2)@C$. The synthesis of $RuO_2@C$ or $Co_3O_4@C$ was similar to that of $(Co_3O_4|RuO_2)@C$ except that no cobalt or ruthenium precursors were used during the synthesis process, respectively. To study the effect of carbon layers on electrochemical activity, $Co_3O_4|RuO_2$, $Co_3O_4$, and $RuO_2$ catalysts were prepared as reference samples. The synthesis process of $Co_3O_4|RuO_2$, $Co_3O_4$, and $RuO_2$ is similar to that of $(Co_3O_4|RuO_2)@C$ except that no oleylamine was contained in the precursor solution. In addition, the $Co_3O_4@C|RuO_2@C$ catalyst was prepared as a reference sample to study the effect of the nanojunction between $Co_3O_4$ and $RuO_2$ on electrochemical activity. For the synthesis of $Co_3O_4@C|RuO_2@C$, 25 μL and 50 μL ruthenium solution were dropped on $Co_3O_4@C$ in two separate steps, each of which was calcinated at 400 $^oC$ for 2 h in a muffle furnace.

**Characterizations:** The crystal structures of $(Co_3O_4|RuO_2)@C$, $RuO_2@/C$ and $Co_3O_4@C$ were characterized by X-ray diffraction (XRD, Bruker) using Cu Kα

radiation. The surface morphology of $(Co_3O_4|RuO_2)@C$ was observed by a field emission scanning electron microscope with an accelerating voltage of 5 kV. Transmission electron microscope (TEM) and energy-dispersive X-ray spectroscopy (EDS) images of $(Co_3O_4|RuO_2)@C$ were collected from a JEOL JEM-F200 instrument. The surface composition and the valence states of samples were characterized by X-ray photoelectron spectroscopy (XPS) using a Thermo Fisher Scientific ESCALAB Xi+ spectrometer equipped with an Al anode as the excitation source. All binding energy was calibrated by using the C 1s peak at 284.8 eV. The Raman spectroscopy was obtained on a Horiba RM HR800 microscope with a 532 nm excitation laser. Inductively coupled plasma-mass spectrometry (ICP-MS) analysis was performed on a PerkinElmer SCIEX ELAN DRCe ICP-MS system to study the stability of $(Co_3O_4|RuO_2)@C$, $RuO_2@C$ and $Co_3O_4|RuO_2$ electrocatalyst. The solution used for the ICP-MS test comes from the electrolyte in the PEM electrolyzer. Thermogravimetric analysis (TGA) was carried out at a rate of 5 °C/min with air flow at 50 mL/min over 30 °C to 800 °C in a STA7200 Instrument.

**Electrochemical measurements:** Oxygen evolution reaction (OER) tests were conducted in a three-electrode electrochemical cell at 25 °C. The Ti felt electrode, an $Hg/Hg_2SO_4$ electrode and a graphite rod served as the working electrode, reference electrode and counter electrode, respectively. All potentials reported are calibrated to reversible hydrogen electrode by the formula:

$$E_{RHE} = E_{Hg/Hg_2SO_4} + 0.652\,V + 0.059 \times pH$$

The OER experiment was measured via linear sweep voltammetry (LSV), electrochemical impedance spectroscopy (EIS), cyclic voltammetry (CV), and Tafel slope. The LSV with a scan rate of 10 mV/s was performed in a 0.1 M $HClO_4$ solution. The electrochemical impedance spectroscopy (EIS) curves were measured in a frequency range of 0.5 to 1000000 Hz at a potential of 1.46 V *vs.* RHE. The electrochemically active surface area (ECSA) was calculated from the CV curves at potential windows with various scan rates (5, 10, 20, 40, and 60 mV/s). The CV with a scan rate of 50 mV/s was used to assess the difference in redox peaks. The pH-

independent measurement was carried out by CVs at different pH values (0.155, 0.398, 0.699). The competition reactions of OER and MOR were studied by LSVs in different media (0.1 M HClO$_4$, 0.1 M HClO$_4$ + 0.1 M CH$_3$OH, 1.0 M HClO$_4$ + 0.1 M CH$_3$OH). The stability tests of catalysts were carried out using CV testing and constant current electrolysis (CPE). In the three-electrode system, the curves of LSV after 3000 cycles CVs and CPE results were collected to evaluate the durability of the electrocatalyst. To further assess the durability of (Co$_3$O$_4$|RuO$_2$)@C for acid OER, a cell test was conducted by using a proton exchange membrane (PEM) electrolyzer. (Co$_3$O$_4$|RuO$_2$)@C on Ti felt was used as the anode, while Pt/C on CP (20 wt%, 0.5 mg/cm$^2$) was used as the cathode. A Nafion 117 PEM was used to transport protons and separate the anode and cathode. In the process of testing, the electrolyte solution (0.1 M HClO$_4$) was supplied by a peristaltic pump. For the measurement of Faradaic efficiency, a sealed cell with three-electrode system was used and the electrolyte solution was purged with N$_2$ before the experiment. The products obtained from CPE test at different time were quantitatively analyzed by high-performance liquid chromatography (HPLC, NP-GC-901A).

**DFT calculations:** The DFT calculations were performed using the Vienna ab initio simulation package (VASP). The Perdew-Burke-Ernzerh (PBE) generalized gradient approximation (GGA) functional was used for the exchange-correlation potential. The energy cutoff was set to 450 eV, and a Monkhorst-Pack mesh of 1 × 1 × 1 was used in K-sampling. To assess the effect of heterogeneous structures on OER activity, the heterostructured (Co$_3$O$_4$|RuO$_2$)@C model was constructed by building Co$_3$O$_4$ (311) on RuO$_2$ (101) based on the HRTEM images. The RuO$_2$@C and Co$_3$O@C models were constructed by RuO$_2$ (101) and Co$_3$O$_4$ (311) surfaces, respectively. The adsorption energy of the adsorbate species on the surface for materials was determined using the following equation:

$$\Delta G_1 = E(OH^*) - E(^*) - E_{H_2O} + \frac{1}{2}E_{H_2} + (\Delta ZPE - T\Delta S) - eU$$
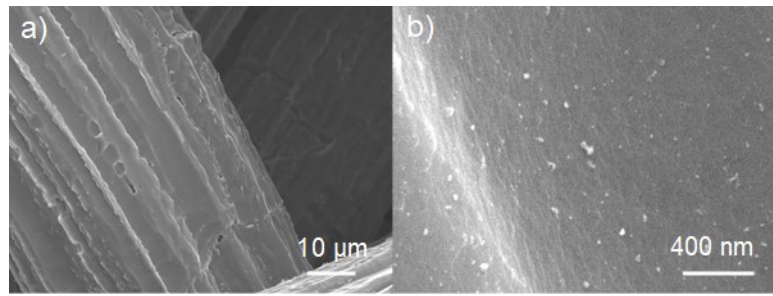
$$\Delta G_2 = E(O^*) - E(HO^*) + \frac{1}{2}E_{H_2} + (\Delta ZPE - T\Delta S) - eU$$

$$\Delta G_3 = E(HOO^*) - (O^*) - E_{H_2O} + \frac{1}{2}E_{H_2} + (\Delta ZPE - T\Delta S) - eU$$
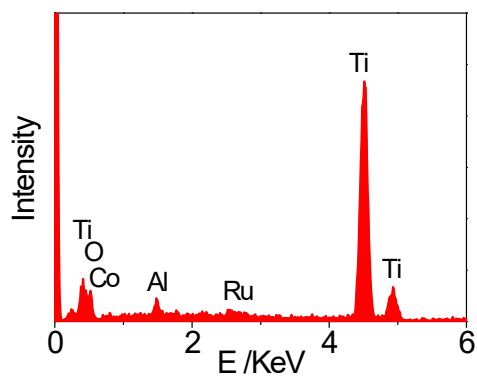
$$\Delta G_4 = E(^*) - E(HOO^*) + E_{O_2} + \frac{1}{2}E_{H_2} + (\Delta ZPE - T\Delta S) - eU$$
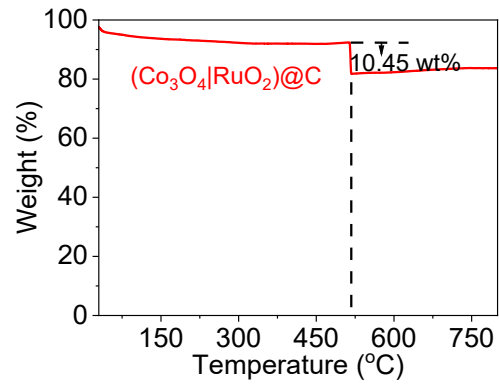
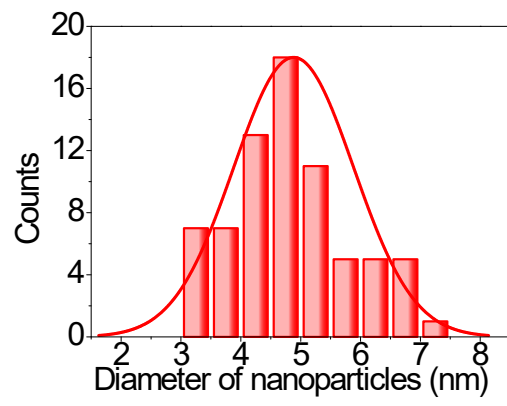**Fig. S1**. TGA profile of $(Co_3O_4|RuO_2)@C$ in the air.

**Fig. S2**. a) SEM image and b) the enlarged SEM image of acid-treated Ti felt.

**Fig. S3**. The EDX of $(Co_3O_4|RuO_2)@C$.
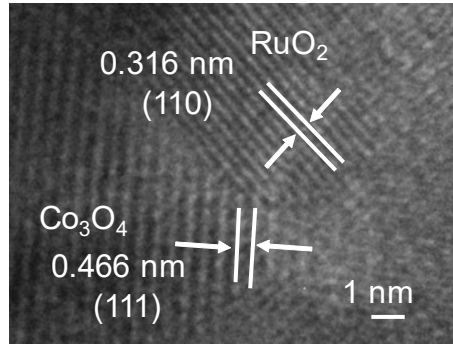
**Fig. S4**. The size distribution of nanoparticles of $(Co_3O_4|RuO_2)@C$.

**Fig. S5**. HRTEM image of (Co$_3$O$_4$|RuO$_2$)@C.

It can be found that the interplanar distance of 0.241 nm for $Co_3O_4$@C in Fig. S6a corresponded to the (311) plane of the $Co_3O_4$ phase, while the interplanar distance of 0.315 nm for $RuO_2$@C in Fig. S6b corresponded to the (110) plane of the $RuO_2$ phase. Both $Co_3O_4$ in $Co_3O_4$@C and $RuO_2$ in $RuO_2$@C were encapsulated by amorphous carbon layers, as indicated by the arrows in the images.
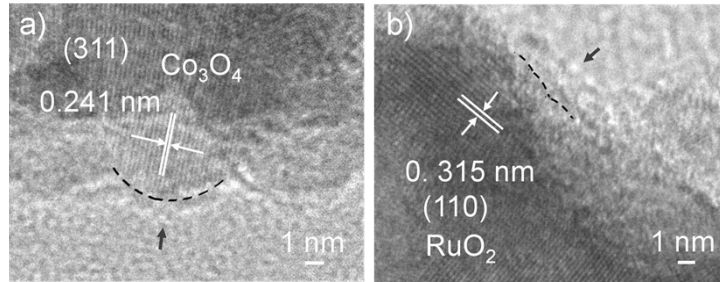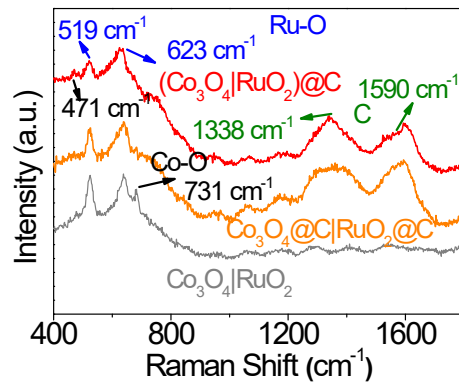


**Fig. S6**. HRTEM images of a) $Co_3O_4$@C and b) $RuO_2$@C, respectively.
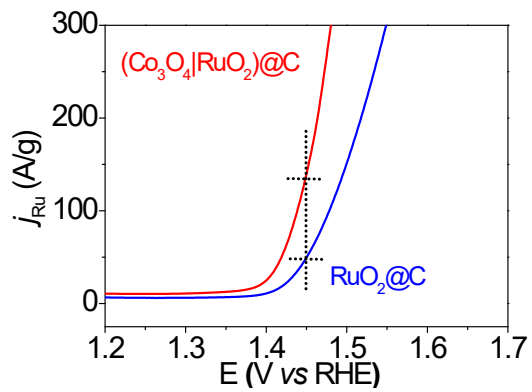
**Fig. S7**. LSV curves normalized by the theoretical loading of Ru for (Co$_3$O$_4$|RuO$_2$)@C and RuO$_2$@C, respectively.
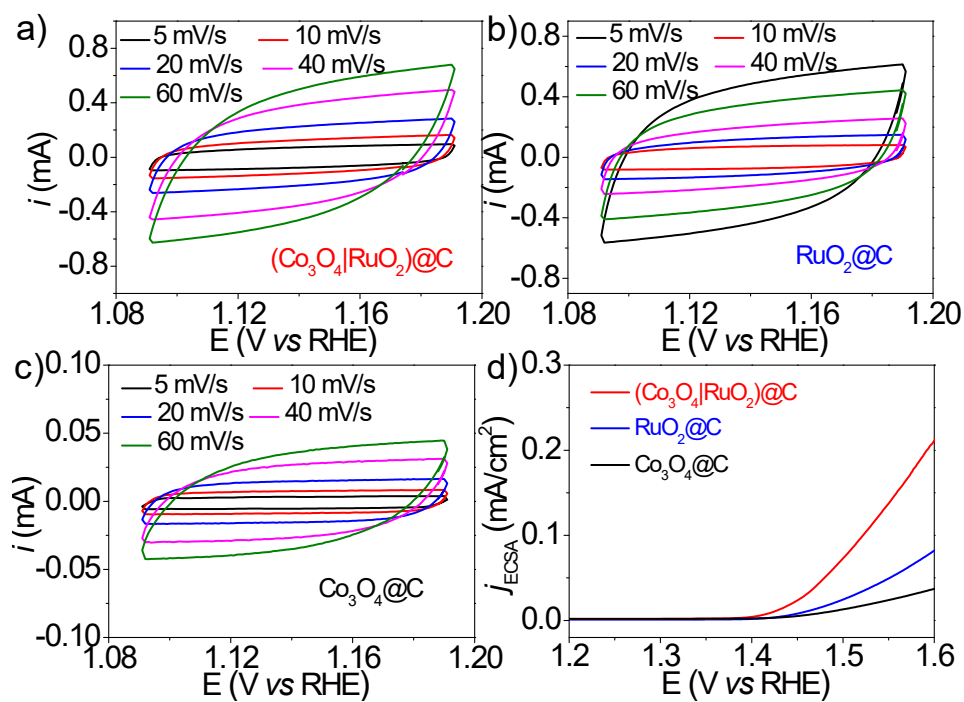
**Fig. S8**. The CV curves of a) $(Co_3O_4|RuO_2)@C$, b) $RuO_2@C$, and c) $Co_3O_4@C$ recorded in the non-Faradaic potential region at different scan rates. d) LSV curves normalized by ECSA for $(Co_3O_4|RuO_2)@C$, $RuO_2@C$ and $Co_3O_4@C$, respectively.

**Fig. S9**. Raman spectra of $(Co_3O_4|RuO_2)@C$, $Co_3O_4@C|RuO_2@C$ and $Co_3O_4|RuO_2$.

The HRTEM image of $Co_3O_4@C|RuO_2@C$ in Fig. S10a displayed the $RuO_2$ (110) plane, $Co_3O_4$ (220) plane and amorphous carbon. Notably, no heterointerface was observed between the $Co_3O_4$ and $RuO_2$ phases, which was due to the sequential oxidation of Co and Ru during calcination. As for $Co_3O_4|RuO_2$ (Fig. S10b), it exhibited $RuO_2$ (110) and $Co_3O_4$ (220) plane, which formed a distinctive nanoscale heterointerface. However, no amorphous carbon layers were presented at the edge of $RuO_2$ (110) and $Co_3O_4$ (220) planes.
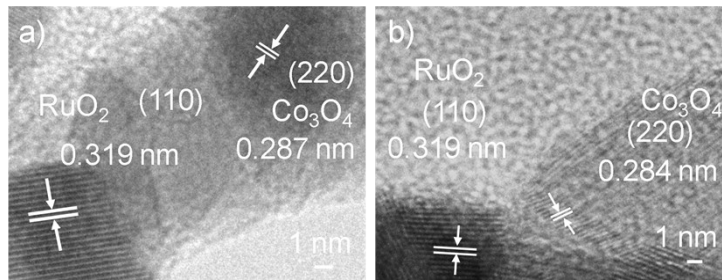


**Fig. S10**. HRTEM images of a) $Co_3O_4@C|RuO_2@C$ and b) $Co_3O_4|RuO_2$, respectively.

The XPS survey spectra (Fig. S11) clearly demonstrated the presence of elemental Co and Ru in $Co_3O_4@C|RuO_2@C$ and $Co_3O_4|RuO_2$. In Fig. S11a, the peaks at 281.3 and 285.6 eV were indexed to $Ru^{4+}$ $3d_{5/2}$ and $Ru^{4+}$ $3d_{3/2}$, respectively. In Fig. S11b, the peaks at 780.1 and 795.2 eV were indexed to $Co^{3+}$ $2p_{3/2}$ and $Co^{3+}$ $2p_{1/2}$, and the peaks at 781.9 and 797.1 eV were indexed to $Co^{2+}$ $2p_{3/2}$ and $Co^{2+}$ $2p_{1/2}$, respectively. As for $Co_3O_4|RuO_2$, the peaks at the peaks at 281.7 and 285.9 eV were indexed to $Ru^{4+}$ $3d_{5/2}$ and $Ru^{4+}$ $3d_{3/2}$, respectively (Fig. S11c). The peaks at 780.8 and 795.5 eV are indexed to $Co^{3+}$ $2p_{3/2}$ and $Co^{3+}$ $2p_{1/2}$, and the other two peaks at 782.4 and 797.6 eV are assigned to $Co^{2+}$ $2p_{3/2}$ and $Co^{2+}$ $2p_{1/2}$, respectively. (Fig. S11d). Obviously, the binding energy of Ru 3d and Co 2p presented the characteristic feature of $Ru^{4+}$ in $RuO_2$ and $Co^{2+}/Co^{3+}$ in $Co_3O_4$. Moreover, it should be noted that the Ru 3d and Co 2p XPS spectra in $Co_3O_4@C|RuO_2@C$ and $Co_3O_4|RuO_2$ both exhibited higher binding energy than those in the $(Co_3O_4|RuO_2)@C$. This observation provided further evidence that the electronic structure of $(Co_3O_4|RuO_2)@C$ was synergistically tuned by the presence of heterointerfaces and the carbon layer, contributing to its enhanced OER performance.
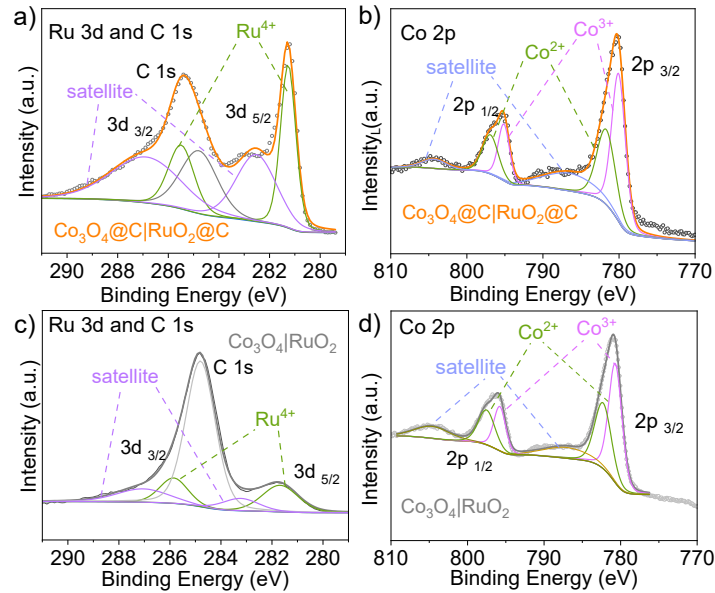


**Fig. S11**. High-resolution XPS spectra of a) Ru 3d and b) Co 2p for $Co_3O_4@C|RuO_2@C$. High-resolution XPS spectra of c) Ru 3d and d) Co 2p for $Co_3O_4|RuO_2$.

The Nyquist plots in **Fig. S12** were derived from electrochemical impedance spectroscopy (EIS) obtained at 1.46 V *vs.* RHE. As two independent semicircles are observed, two parallel components, including a polarization resistance and a constant phase element (CPE), were fitted in series with a resistance ($R_s$) from the solution and all ohmic contact. Among them, $R_{ct}$, which is related to the electrocatalytic kinetics, with a smaller value represents a faster reaction rate. It can be found that the $(Co_3O_4|RuO_2)@C$ possessed a lower charge-transfer resistance of 11.64 Ω (**Table S4**) than that of $Co_3O_4|RuO_2$ ($1.61*10^9$ Ω, **Table S4**), but higher than that of $Co_3O_4@C|RuO_2@C$ (2.87 Ω, **Table S4**), revealing carbon layer contributed to faster charge transfer during the catalysis process.
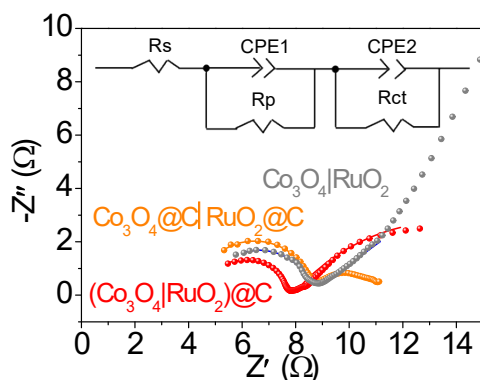


**Fig. S12**. Nyquist plots of $(Co_3O_4|RuO_2)@C$, $Co_3O_4@C|RuO_2@C$ and $Co_3O_4|RuO_2$. The inset was the corresponding equivalent electric circuit.
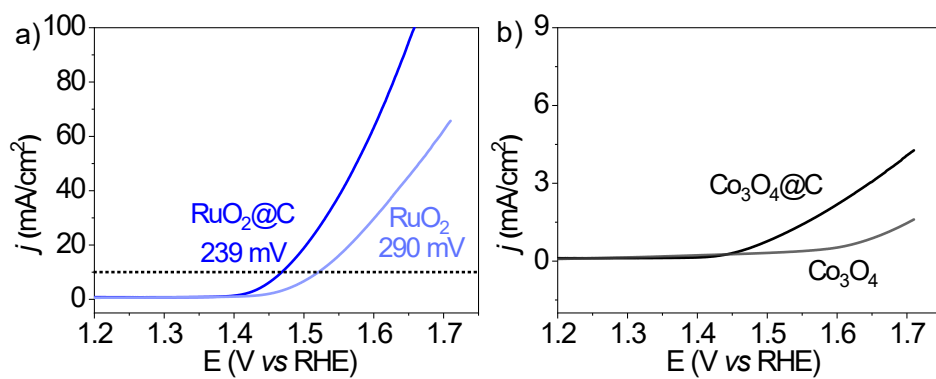
**Fig. S13**. LSV curves of a) $RuO_2$ and $RuO_2@C$ as well as b) $Co_3O_4$ and $Co_3O_4@C$.
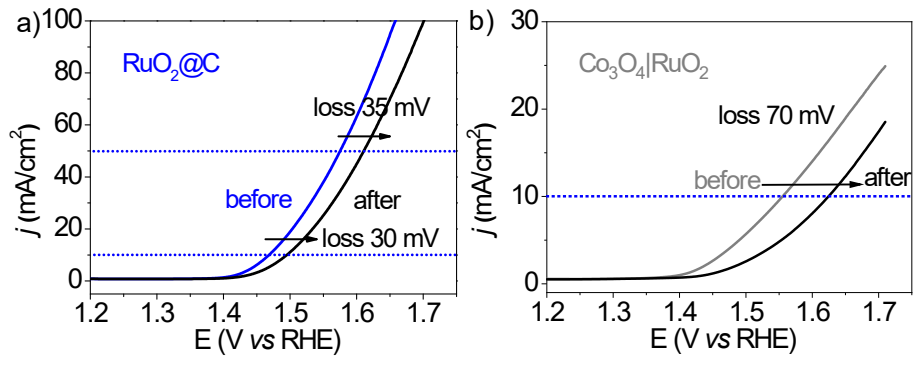
**Fig. S14**. Comparison of attenuation after 4000 cycles for a) RuO$_2$@C and b) Co$_3$O$_4$|RuO$_2$.
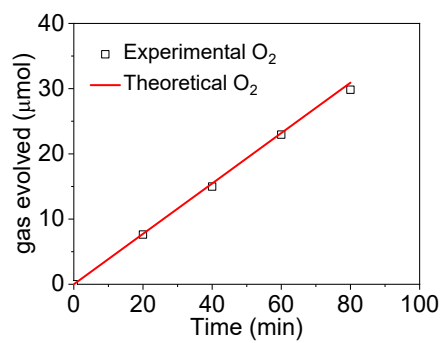
**Fig. S15.** Experimental and theoretical amounts of $O_2$ evolved during the chronopotentiometry electrolysis of the $(Co_3O_4|RuO_2)@C$ catalyst for OER at 10 mA/cm$^2$.
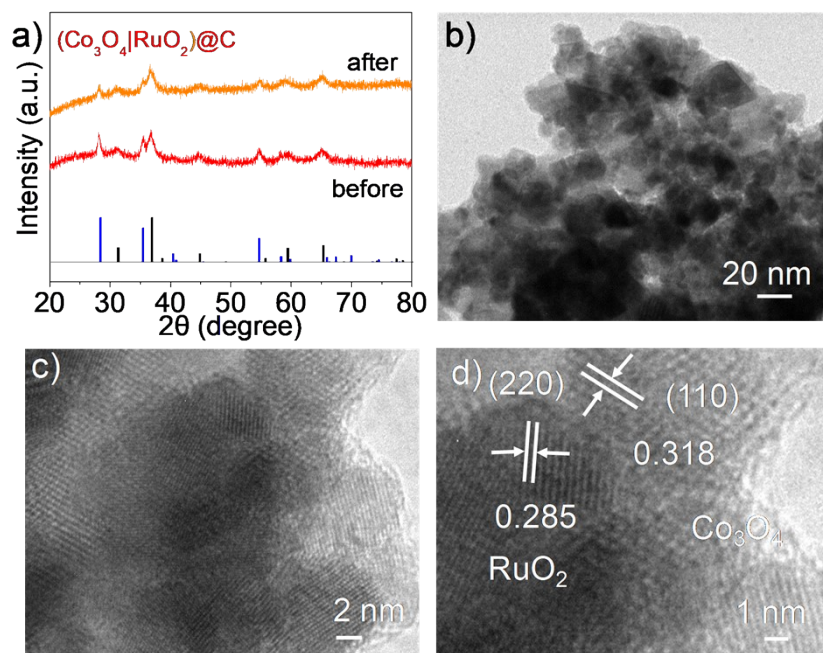
**Fig. S16**. The a) XRD patterns and b-d) TEM images of $(Co_3O_4|RuO_2)@C$ after the OER test.
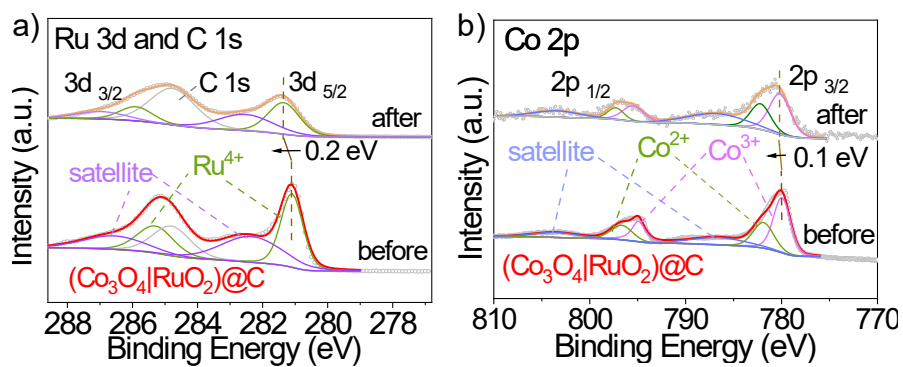
**Fig. S17**. XPS spectra of $(Co_3O_4|RuO_2)@C$ for a) Ru 3d and b) Co 2p before and after the OER test.

It can be seen that the current of $(Co_3O_4|RuO_2)@C$ catalyst remains nearly constant across different pH values (Fig. 5b and S18). In contrast, the current of $RuO_2@C$ catalyst increases as the pH value decreases (Fig. 5c and S18). Thus, the pH-independent OER kinetics exhibited by $(Co_3O_4|RuO_2)@C$ suggested a potential adsorbate evolution mechanism (AEM) mechanism. It is because the AEM mechanism involves four proton-coupled electron transfer pathways: 1) a water molecule is adsorbed on the active surface site of catalyst and one proton of a water molecule and one electron of catalytic site are released to form the M-OH intermediate; 2) one proton and one electron of M-OH are released to form the M-O intermediate; 3) another water molecule nucleophilically attacks M-O to generate an M-OOH intermediate, simultaneously accompanied by the release of one proton and one electron; 4) in the MOOH intermediate, three electrons of OOH anion transfer to M cation to regenerate active sites and release oxygen molecules. In the meantime, one proton and one electron are released. Each step in this process is an electron-proton coupled transfer process, resulting in a pH-independent OER activity.
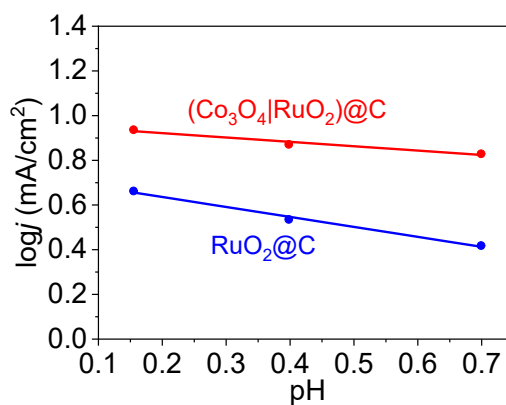


**Fig. S18**. pH dependence on the OER potential at 1.45 V *vs.* RHE for $(Co_3O_4|RuO_2)@C$ and $RuO_2@C$.

It is well known that MOR and OER are competition reactions during the electrolysis process. Compared with the OER process, the MOR process is preferred on the OH* covered surface. After OH* on the surface of the catalyst is deprotonated, the OER process is preferred. As for $(Co_3O_4|RuO_2)@C$ and $RuO_2@C$, two intersection points were observed between the OER curve and the MOR curves obtained by adding different concentrations of methanol solution. Before and after the intersection, the reactions were dominated by MOR and OER, respectively. The overpotential at the intersection points of $(Co_3O_4|RuO_2)@C$ is lower than that of $RuO_2@C$. Therefore, for $(Co_3O_4|RuO_2)@C$, the deprotonation process of OH* on its surface occurred at low overpotential, thus favoring the OER process. While for $RuO_2$, the deprotonation of OH* is more difficult than $(Co_3O_4|RuO_2)@C$, indicating that the MOR process is more favored occurred on the surface of $RuO_2$. Thus, it can be concluded that the construction of $Co_3O_4|RuO_2$ heterojunction decreases surface coverage of OH* and accelerates deprotonation of OH* based on such experimental results.
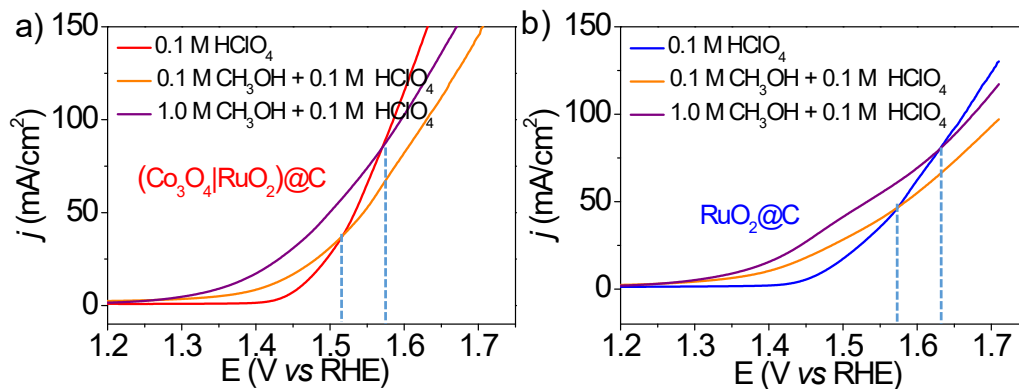


**Fig. S19**. The MOR and OER performance of a) $(Co_3O_4|RuO_2)@C$ and b) $RuO_2@C$. The iR compensation is 60%.
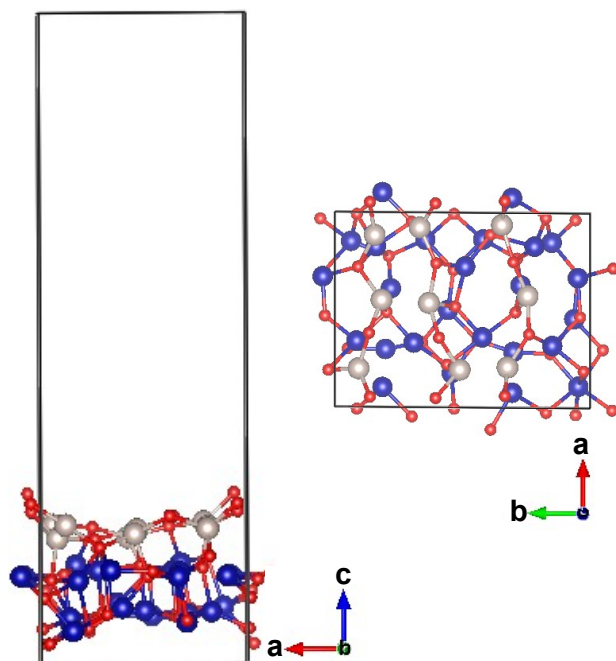
**Fig. S20**. Structural diagram of $(Co_3O_4|RuO_2)@C$ through (311) crystal facet for $Co_3O_4$ and (101) crystal facet for $RuO_2$. Grey, blue, and red spheres represent the Ru, Co and O atoms, respectively.
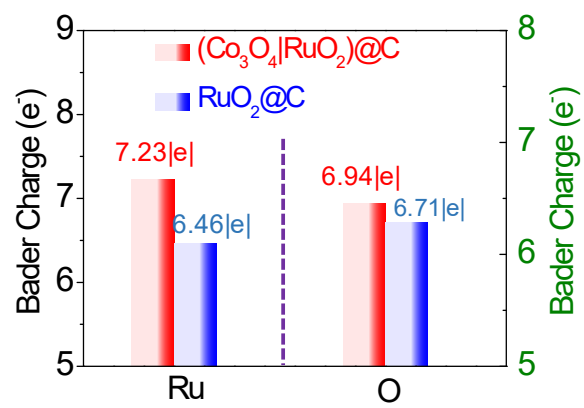
**Fig. S21**. Bader charge for Ru and O in $(Co_3O_4|RuO_2)@C$ and $RuO_2@C$.
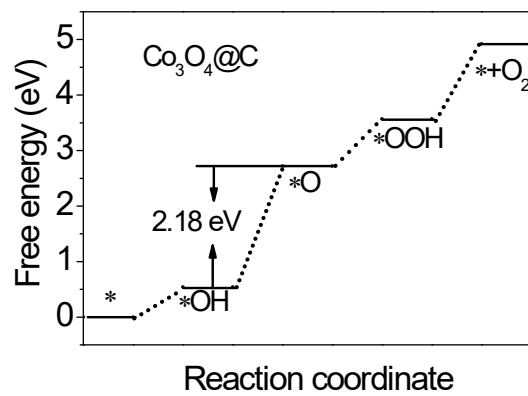
**Fig. S22**. Gibbs free-energy diagram for OER on the Co site for $Co_3O_4@C$.

**Table S1.** Element analysis result (wt %) tested from EDX of $(Co_3O_4|RuO_2)$@C. and $(Co_3O_4|RuO_2)$@C.

| Sample | element | Weight % |
|---|---|---|
| **$(Co_3O_4\|RuO_2)$@C** | O | 27.57 |
| | Ti | 71.00 |
| | Al | 0.38 |
| | Co | 0.35 |
| | Ru | 0.66 |
| | C | 0.04 |

**Table S2.** The integrated area of the Co 2p peak from the XPS spectra of $Co_3O_4$@C and $(Co_3O_4|RuO_2)$@C (Fig. 2c).

| Sample | $Co^{3+}$ | $Co^{2+}$ | $Co^{2+}/Co^{3+}$ |
|---|---|---|---|
| $Co_3O_4$@C | 27300 | 19447 | 0.71 |
| $(Co_3O_4|RuO_2)$@C | 58177 | 32604 | 0.56 |

**Table S3.** Comparison of OER performance in acid electrolytes for $(Co_3O_4|RuO_2)@C$ and recently reported high-efficient Ru-base electrocatalysts.

| Catalysts | Electrolyte | Tafel slope (mV/dec) | Overpotential (mV) | stability test | Reference |
|---|---|---|---|---|---|
| $(Co_3O_4|RuO_2)@C$ | 0.1 M HClO$_4$ | 62 | 202 ($\eta_{10}$) | 300 h (10 mA/cm$^2$); 100 h (50 and 100 mA/cm$^2$) | This work |
| Ru/Co240/Ti | 0.5 H$_2$SO$_4$ | / | 240 ($\eta_{10}$) | decreased from 47.1 mA/cm$^2$ to 37.9 mA/cm$^2$ by the 500th cycle. | 1 |
| RuO$_2$/(Co,Mn)$_3$O$_4$ | 0.5 H$_2$SO$_4$ | 77.0 | 270 ($\eta_{10}$) | 131 mV increase in 24 h (10 mA/cm$^2$) | 2 |
| Ru/Co-N-C-800 °C | 0.5 M H$_2$SO$_4$ | 67.5 | 232 ($\eta_{10}$) | 24 h (10 mA/cm$^2$) | 3 |
| Ru$_x$Co$_{1-x}$O$_y$ | 1.0 M HClO$_4$ | 40.1 | 215 ($\eta_{10}$) | 10 h (10 mA/cm$^2$) | 4 |
| CoO$_x$/RuO$_x$-CC | 0.5 H$_2$SO$_4$ | 61.2 | 180 ($\eta_{10}$) | 60 h (10 mA/cm$^2$) | 5 |
| Ru$_{0.9}$(NiCo$_{1.5}$)$_{0.1}$O$_\delta$ | 0.1 M HClO$_4$ | 32 | ~270 (10) | 5 h at 1.58 V (vs RHE) | 6 |
| RuCo oxide-16-300 50 µg/cm$^2$ | 0.1 M HClO$_4$ | / | 300 ($\eta_{10}$) | Retention of current density 70 % at 1.3-1.65 | 7 |

| | | | | V (vs. RHE) after 500 CV cycles | |
|---|---|---|---|---|---|
| $Ru_{0.258}Ti_{0.736}Zn_{0.006}O_x$ | 0.5 $H_2SO_4$ | 53 | 220 ($\eta_{20}$) | 1.3 V (vs. Ag/AgCl) over 500 cycles | 8 |
| $(Mn_{0.94}Ru_{0.06})O_2$:2.5F | 0.5 $H_2SO_4$ | 62 | 257 ($\eta_{10}$) | 15 h (10 mA/cm$^2$) with an increase in overpotential of 38 mV. | 9 |
| $Mn-RuO_2$ | 0.5 $H_2SO_4$ | 96.7 | 158 ($\eta_{10}$) | ~Stable for about 10 h | 10 |
| $RuNi_2$©G-250 | 0.5 $H_2SO_4$ | 65 | 210 ($\eta_{10}$) | 24 h | 11 |
| Co-RuIr | 0.1 M $HClO_4$ | 66.9 | 235 ($\eta_{10}$) | 25 h (10 mA/cm$^2$) | 12 |
| Ru@FLC-800 | 0.5 M $H_2SO_4$ | 53.1 | 258 ($\eta_{10}$) | 24 h (10 mA/cm$^2$) unchanged | 13 |
| RCO-16-300 | 0.1 M $HClO_4$ | - | 270 ($\eta_{10}$) | - | 14 |
| FeCoNiIrRu/CNFs | 0.5 M $H_2SO_4$ | 153 | 241 ($\eta_{10}$) | 12 h (10 mA/cm$^2$) | 15 |
| Co-IrRu/C | 0.1 M $HClO_4$ | 83 | 248 ($\eta_{10}$) | CV cycling for 3000 cycles | 16 |
| $RuO_2$@$Co_3O_4$ (1:6) | 0.5 M $H_2SO_4$ | 73 | 219 ($\eta_{10}$) | - | 17 |

| np-UHEA12 | 0.5 M $H_2SO_4$ | 84.2 | 258 ($\eta_{10}$) | 40000 s (10 mA/cm$^2$) | 18 |

**Table S4.** EIS fitting results of the components in the circuit from Fig. S12.

| Sample | $R_s$ ($\Omega$) | $R_{ct,1}$ ($\Omega$) | $CPE_1$-p ($\Omega$) | $R_{ct,2}$ ($\Omega$) | $CPE_2$-p ($\Omega$) |
|---|---|---|---|---|---|
| ($Co_3O_4$\|$RuO_2$)@ C | 4.26 | 3.63 | 0.79 | 11.64 | 0.56 |
| $Co_3O_4$@C\|$RuO_2$ @C | 4.28 | 4.25 | 0.95 | 2.87 | 0.64 |
| $Co_3O_4$\|$RuO_2$ | 4.29 | 4.41 | 0.81 | $1.61*10^9$ | 0.48 |

**Table S5.** Desorption energy of proton on OH* and OOH* in the four-step reaction for $(Co_3O_4|RuO_2)@C$ and $RuO_2@C$.

| Sample | OH* (eV) | OOH* (eV) |
|---|---|---|
| $(Co_3O_4|RuO_2)@C$ | 1.02 | 1.41 |
| $RuO_2@C$ | 1.13 | 1.57 |

# References

[1]     J. Y. Kim, H. Park, H. Kim, E. Hwang, S. H. Ahn, S. -K. Kim and Bull. Korean，Electrochemical preparation of Ru/Co bi-layered catalysts on Ti substrates for the oxygen evolution reaction, *Chem. Soc.* 2016, **37,** 1270-1277.

[2]     S. Q. Niu, X. -P. Kong, S. W. Li, Y. Y. Zhang, J. Wu, W. W. Zhao and P. Xu, Low Ru loading $RuO_2/(Co,Mn)_3O_4$ nanocomposite with modulated electronic structure for efficient oxygen evolution reaction in acid, *Appl. Catal. B Environ.* 2021, **297,** 120442.

[3]     C. L. Rong, X. J. Shen, Y. Wang, L. Thomsen, T. W. Zhao, Y. B. Li, X. Y. Lu, R. Amal and C. Zhao, Electronic structure engineering of single-atom Ru sites via $Co-N_4$ sites for bifunctional pH-universal water splitting, *Adv. Mater.* 2022, **34,** 2110103.

[4]     A. Yu, M. H. Kim, C. Lee and Y. Lee, Structural transformation between rutile and spinel crystal lattices in Ru-Co binary oxide nanotubes: enhanced electron transfer kinetics for the oxygen evolution reaction, *Nanoscale* 2021, **13,** 13776-13785.

[5]     L. M. Deng, S. Y. Liu, D. Liu, Y. -M. Chang, L. L. Li, C. S. Li, Y. Sun, F. Hu, H. -Y. Chen, H. Pan and S. J. Peng, Activity-stability balance: the role of electron supply effect of support in acidic oxygen evolution, *Samll* 2023, **19,** 2302238.

[6]     Y. Y. Wu, M. Tariq, W. Q. Zaman, W. Sun, Z. H. Zhou and J. Yang, Ni-Co codoped $RuO_2$ with outstanding oxygen evolution reaction performance, ACS *Appl. Energy Mater.* 2019, **2,** 4105-4110.

[7] H. Han a, I. Kim and S. Park, Cobalt-based oxygen evolution catalyst as active and stable as iridium in acidic media, *Electrochim. Acta* 2020, **344,** 136160.

[8] K. Kishor, S. Saha, M. K. Gupta, A. Bajpai, M. Chatterjee, S. Sivakumar and R. G. S. Pala, Roughened Zn-doped Ru-Ti oxide water oxidation electrocatalysts by blending active and activated passive components, *ChemelectroChem* 2015, **2,** 1839-1846.

[9] D. Kim, A. Voronova, S. Kim, J. Y. Kim, H. -Y. Park, J. H. Jang and B. Seo, Electronic structure modulation of $MnO_2$ by Ru and F incorporation for efficient proton exchange membrane water electrolysis, *J. Mater. Chem. A* 2022, **10,** 21985-21994.

[10] S. Chen, H. Huang, P. Jiang, K. Yang, J. F. Diao, S. P. Gong, S. Liu, M. X. Huang, H. Wang and Q. W. Chen, Mn-Doped $RuO_2$ nanocrystals as highly active electrocatalysts for enhanced oxygen evolution in acidic media, *ACS Catal.* 2020, **10,** 1152-1160.

[11] X. J. Cui, P. J. Ren, C. Ma, J. Zhao, R. X. Chen, S. M. Chen, N. P. Rajan, H. B. Li, L. Yu, Z. Q. Tian and D. H. Deng, Robust interface Ru centers for high-performance acidic oxygen evolution, *Adv. Mater.* 2020, **32,** 1908126.

[12] J. Q. Shan, T. Ling, K. Davey, Y. Zheng and S. -Z. Qiao, Transition-metal-doped RuIr bifunctional nanocrystals for overall water splitting in acidic environments, *Adv. Mater.* 2019, **31,** 1900510.

[13] C. X. Shi, Y. Yuan, Q. Shen, X. D. Yang, B. Q. Cao, B. Xu, B. T. Kang, Y. Q. Sun and C. C. Li, Encapsulated ruthenium nanoparticles activated few-layer

carbon frameworks as high robust oxygen evolution electrocatalysts in acidic media, *J. Colloid Interface Sci.* 2022, **612,** 488-495.

[14] H. Han, I. Kim and S. Park, Cobalt-based oxygen evolution catalyst as active and stable as iridium in acidic media, *Electrochim. Acta* 2020, **344,** 136160.

[15] H. Zhu, Z. F. Zhu, J. C. Hao, S. H. Sun, S. L. Lu, C. Wang, P. M. Ma, W. F. Dong and M. L. Du, High-entropy alloy stabilized active Ir for highly efficient acidic oxygen evolution, *Chem. Eng. J.* 2022, **431,** 133251.

[16] Y. Li, L. Zhao, X. Du, W. T. Gao, C. Zhang, H. Chen, X. He, C. Wang and Z. Q. Mao, Cobalt-doped IrRu bifunctional nanocrystals for reversal-tolerant anodes in proton-exchange membrane fuel cells, *Chem. Eng. J.* 2023, **461,** 141823.

[17] Y. Jiang, H. Liu, Y. M. Jiang, Y. N. Mao, W. Shen, M. Li and R. X. He, Adjustable heterointerface-vacancy enhancement effect in $RuO_2@Co_3O_4$ electrocatalysts for efficient overall water splitting, *Appl. Catal. B Environ.* 2023, **324,** 122294.

[18] Z. -X. Cai, H. Goou, Y. Ito, T. Tokunaga, M. Miyauchi, H. Abe and T. Fujita, Nanoporous ultra-high-entropy alloys containing fourteen elements for water splitting electrocatalysis, *Chem. Sci.* 2021, **12,** 11306-11315.